Available online at www.sciencedirect.com

SciVerse ScienceDirect

Journal of the European Ceramic Society 32 (2012) 2273–2281

www.elsevier.com/locate/jeurceramsoc

Integrated analysis of non-linear loss mechanisms in Yb:YAG ceramics for laser applications

Laura Esposito [a,*], Thierry Epicier [b], Marina Serantoni [c], Andreana Piancastelli [a], Daniele Alderighi [d], Angela Pirri [d], Guido Toci [d], Matteo Vannini [d], Sergiu Anghel [e], Georges Boulon [e]

[a] *Institute of Science and Technology for Ceramic, National Research Council, Via Granarolo 64, I-48018 Faenza, Italy*
[b] *University of Lyon, INSA of Lyon, MATEIS UMR CNRS 5510, Bât. B. Pascal, 69621 Villeurbanne, France*
[c] *Daunia Solar Cell S.r.l., I-47100 Forlì FC, Italy*
[d] *Institute of Applied Physics "Nello Carrara", National Research Council, Via Madonna del Piano 10, 50019 Sesto Fiorentino, Italy*
[e] *Claude Bernard/Lyon1 University, Physical Chemistry of Luminescent Materials Lab., University of Lyon, UMR CNRS 5620, Bât Kastler, 69622 Villeurbanne, France*

Received 20 October 2011; received in revised form 15 February 2012; accepted 27 February 2012
Available online 23 March 2012

Abstract

Transparent 9.8 at% Yb:YAG ceramic samples were prepared by reactive sintering of commercial oxides and using 0 or 1 wt% polyethylene glycol (PEG) as dispersant. The optical quality of the samples turns out to be improved by using a dispersant and optical transmittance close to the commercial samples has been obtained. On the other hand the laser characterization evidenced the activation of a non-linear loss mechanism occurring only in the sample containing PEG and despite its better optical quality, at high excitation level. A SEM analysis of material microstructure could not explain this behavior. A state of the art TEM analysis at nanometric scale was performed providing high resolution chemical spectroscopic results that indicate the presence of amorphous and crystalline silicate phases playing different roles in the two samples.

Keywords: Laser YAG-based ceramics; Electron microscopy; Microstructure; Optical properties; Grain boundaries

1. Introduction

Ceramic laser media fabricated by vacuum sintering are very attractive materials in substitution of single crystal laser materials.[1–3] Between them, the ytterbium-doped yttrium aluminum garnet (Yb:YAG) material is very desirable for the application of diode-pumped solid-state lasers[4] because of the excellent structural and optical properties of this garnet. The optical quality of the achieved ceramic can be limited by the residual porosity, grain boundaries impurities and dopant segregation acting as optical scattering centers.[5,6] Nevertheless, a sample that shows a good optical quality in terms of low scattering and high transmission after a passive optical characterization, can be affected by significant optical losses when operated in a laser cavity at high excitation densities.[7]

Two approaches have been reported in the literature for the production of laser grade transparent ceramics.[1,2] The method described by Yanagitani et al. has been adopted by Konoshima Chemical Co. in Japan. It is based on the chemical synthesis of YAG powder, powder milling, shaping, and finally solid state sintering. The second method is based on the reaction sintering of a stoichiometric mixture of Y_2O_3 and Al_2O_3 powders. The latter method is more convenient from the point of view of the starting materials, since a wide selection of commercial, highly pure Al_2O_3 and Y_2O_3 powders exists, whereas commercial YAG powders are generally highly aggregated and require long milling steps that easily introduces impurities.

In the literature, excellent laser properties has been reported with reactive sintering method, but little is said on the mechanisms governing the phenomena occurring at high temperature, as for example the role of additives used to ease the sintering (generally silica) or to promote a good particle packing during shaping (organics).[8,9] In order to understand these phenomena, in this work the optical and laser properties have been analyzed

* Corresponding author.
E-mail address: laura.esposito@istec.cnr.it (L. Esposito).

0955-2219/$ – see front matter © 2012 Elsevier Ltd. All rights reserved.
doi:10.1016/j.jeurceramsoc.2012.02.047

Table 1
Commercial oxides.

Powder	Producer	SSA (m^2/g)	D_{50} (μm)	Purity (%)	Main impurities (ppm)
Al_2O_3	Taimei	17.22	0.20	>99.99	Si 3; Fe 7; Ca 2; Na, K, Mg 1
Y_2O_3	Nano Cerox	45.2	0.05	>99.99	Na 35; Al 7; Si 60; S 40; P 10; Cl 80; Ca 10; Fe 8
Yb_3O_3	Aldrich	1.78	>1	99.9	Ca 21; Dy 6.1; Er 16

Table 2
Experimental conditions and samples density. The composition of both samples is 9.8 at% Yb:YAG. Green density is the density of as-pressed samples before sintering.

Sample	PEG 400 (wt%)	Linear + CIP (bar)	Green density (g/cm^3)	Calcination cycle (°C × h)	Sintering cycle (°C × h)	Annealing cycle (°C × h)	Final density (g/cm^3)	Linear shrinkage (%)
1	0	2500	2.66	800 × 24	1735 × 16	1300 × 0.5	4.75	17.16
2	1.0	2500	2.71	800 × 24	1735 × 16	1300 × 0.5	4.74	16.93

in connection with the investigation of the microstructure up to the atomic level by means of HR-TEM analyses. We describe the production and the integrated optical and structural analysis of Yb doped YAG ceramic materials obtained by reactive sintering. Although it needs to be investigated deeply, the reactive sintering of stoichiometric mixtures of Y_2O_3 and Al_2O_3 turns out to be faster and cheaper and can provide in principles evenly high quality samples.

In particular we can indicate, after optical and laser characterization and TEM analysis of the samples, a specific role played by the silicate phases introduced by means of the additives used in the samples production, namely TEOS as sintering aid and the PEG 400 as dispersant, in the occurrence of loss mechanisms that can be activated under laser action even in presence of good optical quality of the sample.

2. Experimental

2.1. Sample production

We report two Ytterbium-doped YAG materials with the stoichiometry $Yb_{0.294}Y_{2.706}Al_5O_{12}$, i.e. with 9.8 at% of Yb with respect to the overall Y plus Yb amount, for which TEOS 0.5 wt% was used as sintering aid and polyethylene glycol (PEG 400) was used as dispersant for its surfactant properties.[10,11]

For the reactive sintering process, already illustrated elsewhere,[7] commercial oxides, 3–4 N in purity have been used (see Table 1). The weight loss of the powders was measured as reported in a previous work.[12] The production parameters and the obtained densities of the two samples under investigation are reported in Table 2.

2.2. Optical and laser characterization

Optical transmittance is measured with a UV/IR Lambda 19 Spectrometer, Perkin Elmer Instrument over the wavelength region from 600 to 1200 nm.

The measured transmission (T_M) is given by

$$T_M(\lambda) = T_F(\lambda) \cdot T_S \cdot T_A(\lambda) \quad (1)$$

being $T_F(\lambda)$ the fraction transmitted after multiple Fresnel reflections (calculated), T_S the unscattered fraction and T_A (λ) the unabsorbed fraction. $T_F(\lambda)$ has been calculated by considering the multiple reflections of a collimated beam incident on the plate and by the incoherent summation of the transmitted beams at every order. It can be easily obtained

$$T_F(\lambda) = \frac{(1 - R(\lambda))^2}{1 - R(\lambda)^2} \quad (2)$$

where $R(\lambda)$ is the reflectivity of the air/YAG interface at the wavelength λ.

The scattering and absorption coefficient ($\alpha_{sc,abs}$) has been obtained by the relation

$$\alpha_{sc,abs} = -\frac{1}{d} \ln(T_{S,A}) \quad (3)$$

being d the sample thickness. The scattering transmission T_S can be obtained as average in the range of 600–850 nm, where the absorption of the active ion Yb^{3+} can be neglected. The absorption coefficient α_{abs} can be obtained by (1) and (3) once that T_M and T_S are measured and T_F is calculated.

The laser performance of the ceramic samples was tested using a folded laser cavity (see Fig. 1) optically pumped by a temperature-stabilized, fiber-coupled laser diode delivering about 20 W at the wavelength of 940 nm focused on the sample by a pair of achromatic doublets achieving a Gaussian beam with 130 μm radius at $1/e^2$, which results in a maximum peak absorbed intensity of about 75 kW/cm^2. The laser has been

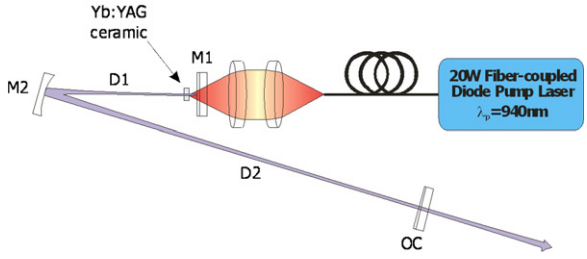

Fig. 1. Setup for laser characterization. The input mirror (M1) and the output coupler are flat, the radius of curvature of the folding mirror (M2) is 100 mm, the distance D1 between M1 and M2 is 55 mm and the distance D2 is 190 mm.

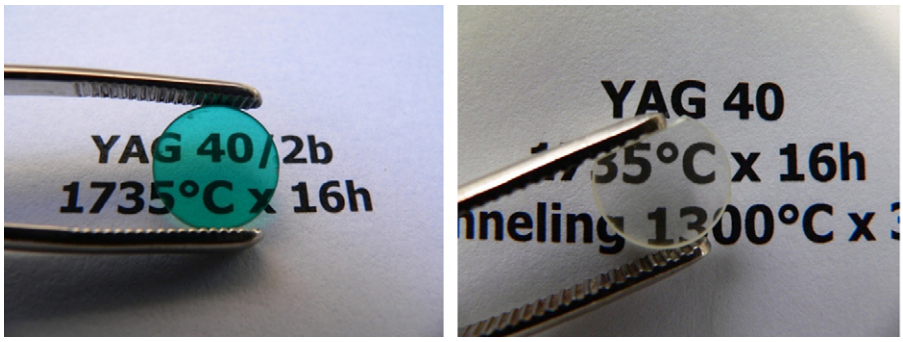

Fig. 2. Optical image of sample 2 before and after annealing in air at 1300 °C × 1 h.

operated in quasi-CW mode, with square pump pulses with a Duty Factor (DF) of 20%, at a repetition rate of 10 Hz. The geometry of the laser cavity has been kept the same over the measurements with the two samples in order to highlight the difference in laser performance due to the samples only. The results can be also compared to that obtained by using commercial high quality Yb doped materials obtained with a similar setup.[5,13] The output coupling of the cavity has been varied by inserting output couplers (OCs) with different transmission in order to change the cavity losses in a controlled way. Due to the operating scheme at normal incidence and the absence of AR coating, the samples have been carefully aligned to re-inject the Fresnel reflection on the cavity axis (for Yb:YAG at 1030 nm $R = 8.46\%$ for single reflection). All the power data reported in this paper refer to the average power divided by the DF (i.e. the average power during the pumping periods).

2.3. TEM analysis

Sample preparation for TEM work was performed by ion-beam thinning of preliminary, carefully grinded samples down to a thickness of about 100 μm. In order to avoid any cause of impurity contamination, no carbon was deposited on the thin foils, although this induced undesirable charging effects reducing the stability of the specimen during exposure to the electron beam. The grain boundary structure and chemical compositions were analyzed at high resolution in a JEOL 2010F microscope operating at 200 kV, and equipped with an INCA-Oxford Instruments EDX analyzer which was used for nanometric probe (i.e. 0.5–3 nm) analysis. In most of experimental spectra, some minor Ti and Cu signals arise from the specimen holder. EELS (Electron Energy-Loss Spectroscopy) measurements were also performed using a Gatan Digi PEELS spectrometer.

3. Results

The two samples analyzed in this study, characterized by the composition 9.8 at% Yb:YAG, are sample 1, prepared with no dispersant, and sample 2, with 1.0 wt% of PEG 400. In Table 2 we report the experimental conditions used for the preparation of the two samples and the results in terms of green and sintered density. The annealing at 1300 °C × 1 h in air assures, by oxygen diffusion into the sample, the Yb^{2+} to Yb^{3+} transformation and the consequent change of the color of the sample from deep green to transparent (see Fig. 2).

3.1. Optical measurement and laser performances

The samples have been investigated by means of both optical and laser characterization that turn out to be complementary and equally important in order to obtain unambiguous indications on the quality of these materials as laser active media, as recently shown.[7]

The visible to IR transmittance and absorption spectra of the two samples are shown in Fig. 3(a) and (b) respectively. In order to highlight only scattering and absorption, the transmittance spectra have been corrected for the wavelength dependent Fresnel reflections on the two uncoated interfaces. In this way

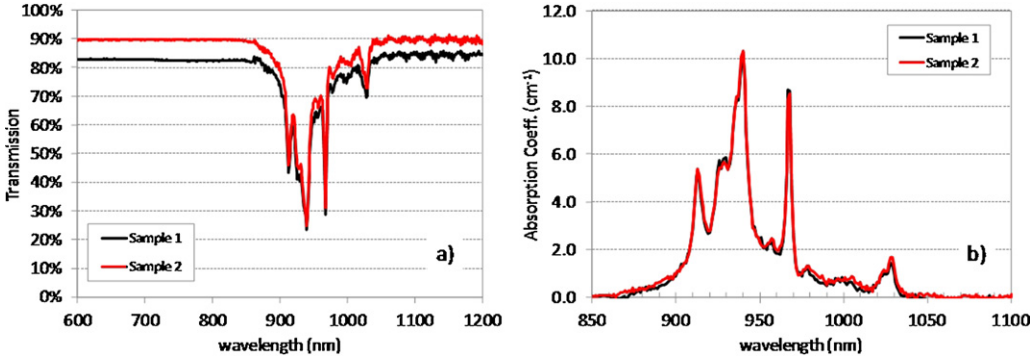

Fig. 3. IR transmission (a) and absorption (b) spectra of the samples. The spectra shown in (a) are corrected for Fresnel reflections.

Table 3
Average transmittance values (Fresnel corrected) in the range of 600–850 nm and corresponding scattering coefficients of the samples.

Sample	Thickness (mm)	Transmittance (%)	Scattering coefficient (cm^{-1})
1	1.22 ± 0.02	82.6 ± 0.21	1.56 ± 0.05
2	1.24 ± 0.02	89.6 ± 0.09	0.88 ± 0.02

the residual baseline in the transmittance spectra represents the unscattered fraction (T_S) which is about wavelength independent.

Table 3 reports the scattering coefficient as obtained from equation (2) by averaging T_S over the spectral range from 600 to 850 nm where the Yb^{3+} ions do not absorb. Sample 2 shows a smaller value for the scattering coefficient α_{sc}, compared with sample 1 and consequently a higher optical quality.

The absorption coefficients of the two samples, reported in Fig. 3(b), are almost undistinguishable as a proof of the equality of doping and of the independency of scattering by the wavelength.

For a deeper insight on the overall quality and performance of the samples the laser performances have also been tested.

In Fig. 4a we report the laser output power as a function of the absorbed pump power obtained for different values of the output coupler transmittance (T_{OC}). It can be observed that for sample 1 the maximum output power increases monotonically for increasing T_{OC} from 1.5% to 39%, showing a maximum slope efficiency of 44% and a maximum absolute efficiency of 29% with respect to the absorbed pump power. In this case the active medium provides the necessary gain to compensate the increase of cavity losses due to the increased T_{OC}. On the other hand, sample 2 shows an increase of the laser output power for increasing the T_{OC} up to 12%, while, for higher values of the T_{OC}, a dramatic roll-over in the output curve appears for increasing pump power. Furthermore, for a given pump power, the output power decrease when T_{OC} increases above 19%. For T_{OC} higher than 39% the laser action is completely absent at any pump power available in our setup. In summary we observed that the sample 2, despite its lower internal losses due to scattering, shows the activation of a non-linear loss mechanism that dramatically decreases the efficiency of laser action. The loss process appears either by increasing the cavity output coupling or by increasing the pump power.

The former observation clearly indicates a specific role of the excitation density, i.e. of the density of ions population in the excited laser manifold, about the activation of the loss mechanism. Indeed, the decrease of the laser slope efficiency for increasing output coupling indicates either a reduction in the quantum efficiency of the lasing ions (i.e. the onset of decay paths alternative to the lasing transition), and/or the occurrence of a nonlinear loss mechanism in the active medium.

Considering that an increase of the cavity output losses produces a corresponding increase of the population inversion in the lasing volume (because of the saturated gain must balance the round trip losses to sustain the laser oscillation), then the activation of the observed loss mechanism appears directly correlated with the increase of the density of the excited ions.

In order to quantitatively evaluate the phenomenon we perform the analysis of the slope behavior as a function of T_{OC} according the following relation[14]

$$\eta_{sl} = \eta_{abs} \frac{\lambda_P}{\lambda_L} \frac{T_{OC}}{T_{OC} + L} \tag{4}$$

where η_{sl} is the slope efficiency respect to the absorbed pump, η_{abs} is the fraction of the absorbed pump that effectively take part to the laser action, λ_P and λ_L are the pump and laser wavelengths, T_{OC} is the output coupler transmission and L is the linear loss per round trip (i.e. for a double pass into the ceramic sample). For the sample 2 the values of η_{sl} has been determined by the linear part of the curve with pump power lower than that where the roll-over occurs. The measured η_{sl} values and the best fitting curves obtained by (4) are shown in Fig. 4b in which the fit for the sample 2 has been calculated excluding the slope value at $T_{OC} = 39\%$. The linear losses L and the absorption efficiency η_{abs}

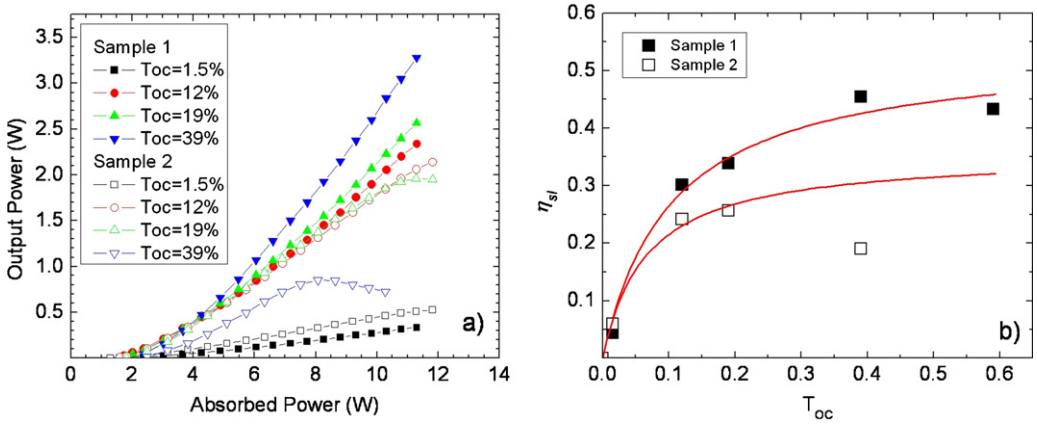

Fig. 4. (a) Laser output power for the sample 1 (solid symbols) and sample 2 (open symbols) as function of the pump power, obtained with different OC transmittance. (b) Experimental values (squares) and calculated (lines) slope efficiency as function of T_{OC}.

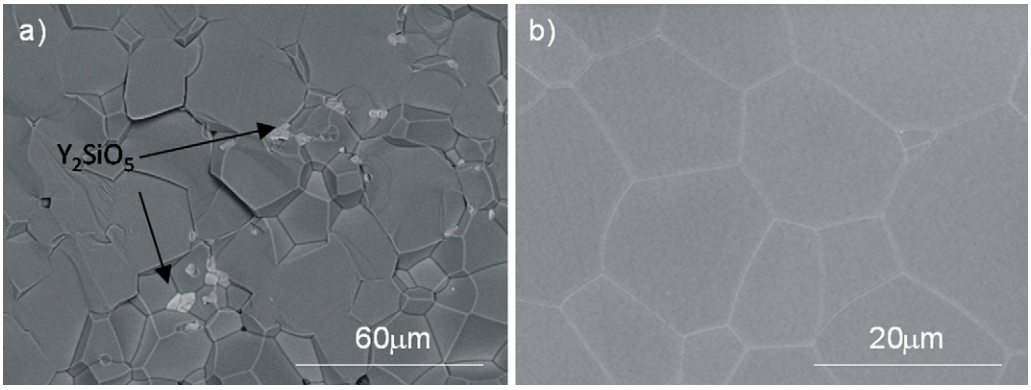

Fig. 5. (a) SEM back scattered image of the fracture surface of a sample with composition of sample 1 sintered at 1650 °C × 16 h and (b) microstructure of the polished surface of sample 2.

have been used as fitting parameters. We obtain, respectively for sample 1 and sample 2, $L = 10.3\%$ and 6.5% and $\eta_{abs} = 59\%$ and 39%. Respect to the values previously reported for the scattering losses (17.4% and 10.4% in single pass respectively for the two samples, that have to be doubled in order to evaluate the round trip losses), the values of L are considerably lower. This is due to the fact that the laser characterization has been performed on the area with best output, which corresponds to a pumped spot with a diameter of 130 μm, while the transmittance has been measured on a spot several mm^2 wide. Consistently with the scattering data, the linear losses are lower in the sample 2 even at the 100 μm scale. What can be observed is the lower pump efficiency of the sample 2 respect to the sample 1, indicating that, even below the pump level at which the roll-over is observed, the non linear loss channel is already active.

Further investigation will be carried out in future works to clarify the specific role of the thermal load in the observed dynamics even if in the present analysis the two samples undergo almost the same thermal load, being their pump absorption strictly comparable (48% and 51% for the samples 1 and 2 respectively).

It must be noticed that the observed nonlinear loss mechanism cannot be attributed only to thermal effects, because in this case it should appear for a given pump power for all the values of T_{OC}; conversely, the output curves obtained with T_{OC} of 1.5% and 12% does not show any occurrence of an additional loss mechanism. In order to understand the nature of the observed non-linear loss channel, the two samples have been investigated by SEM and TEM.

3.2. SEM analyses

An example of the fractured and polished surfaces after sintering is reported in Fig. 5. A quite large average grain size (>20 μm) is observed in both samples, with larger grain size in the sample 2 respects to the sample 1. Only few small pores (size < 2 μm) and few grains (2–4 μm) with a composition that approximately corresponds to Y_2SiO_5 were found with SEM EDS analyses, with an overall amount that is larger in sample 1 than in sample 2. An example of Y_2SiO_5 aggregated grains is shown in Fig. 5(a) for a sample with the same composition as sample 1 but sintered at a lower temperature. These results, due to the big difference in the refractive index between YAG and Y_2SiO_5, can account for the higher scattering losses observed in the sample 1, but still do not account for the results obtained in the laser characterization.

3.3. TEM analyses

The two samples were observed in TEM in order to understand if the origin of the difference in the laser performances could be found at the nanometric scale. In Figs. 6 and 7 TEM images and EDS analyses are reported for samples 1 and 2 respectively. A systematic Si enrichment is observed at grain-boundaries as shown in Figs. 6(c) and 7(c). Furthermore, intergranular phases are observed in both samples. For sample 1 the composition deduced from the spectrum shown in Fig. 6(c) is about $O_{0.61}Al_{0.16}Y_{0.15}Si_{0.08}$. EELS analysis, which reflects the atomic structure through the shape of core-loss edges, indicates the resemblance of this phase with vitreous SiO_2. Accordingly, the measured composition can be interpreted as the result of a superposition of two contributions: that of the glassy phase and that from the adjacent YAG grains, due to the limited spatial resolution of the EDX. Mixing the formulae SiO_2 and $Y_3Al_5O_{12}$ in adequate proportions leads to the composition $O_{0.61}Al_{0.12}Y_{0.20}Si_{0.07}$, which is reasonably close to what has been measured.

Moreover, frequent crystalline films are also observed at grain boundaries. A typical example is shown in Fig. 6(d), where a more or less continuous layer, with a thickness of about 2–5 nm, is observed. Such narrow intergranular phases could not be detected by SEM. A significant silicon enrichment is measured in EDX (Fig. 6(e)). Furthermore, indexing of the diffraction pattern obtained after Fourier transform of the HRTEM micrograph (so-called diffractogram) evidences the yttrium orthosilicate Y_2SiO_5 monoclinic phase (space group C2/c with $a = 1.2501$ nm, $b = 6.7282$ Å, $c = 10.4217$ Å, $\beta = 102.68°$[15]). Similar Y_2SiO_5 crystallites were also identified in sample 2 (Fig. 7(d)). The analysis of data obtained from the EDX measurement shown in Fig. 7(e) clearly supports the Y_2SiO_5 composition (see Table 4). The size of the Y_2SiO_5 grains identified by TEM analyses is of the order of few nm, much

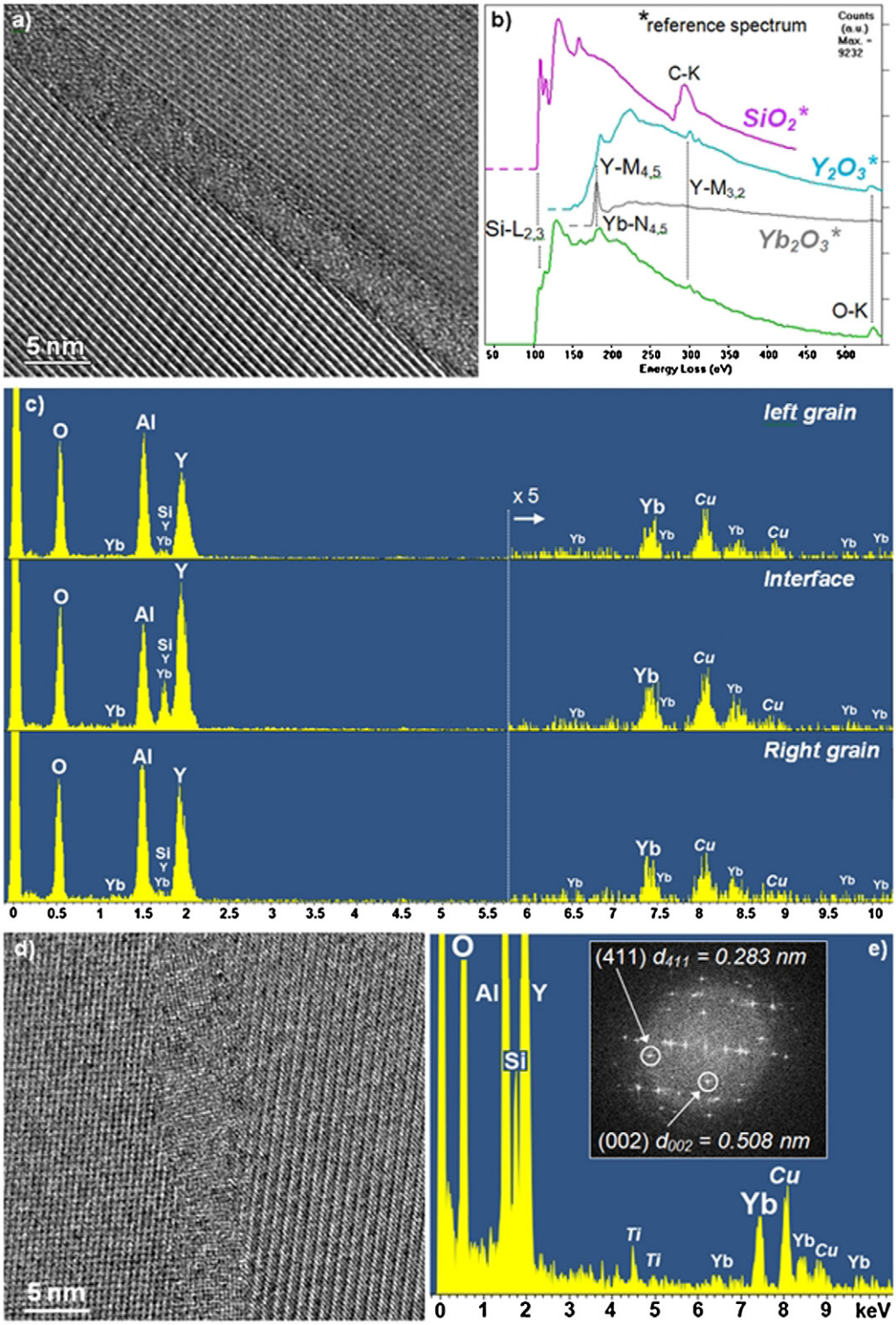

Fig. 6. Summary of TEM and EDX result for sample 1. (a) Representative grain boundary exhibiting a continuous non-crystalline layer. (b) EELS analysis of the film shown in (a) (bottom spectrum, obtained with a 0.8 nm electron probe in order to minimize the contribution of YAG grains to the recorded signal). Reference spectra from pure silica (SiO_2)[23] commercial Y_2O_3 and Yb_2O_3 powders are shown for comparison. (c) EDX spectra (X-ray counts vs. energy) from nano-probe measurements on the interface and at about 5 nm from it within adjacent grains. (d) HRTEM image of a Y_2SiO_5 crystalline intergranular layer. (e) EDX spectrum of the Y_2SiO_5 crystalline phase. Inset is a diffraction identification of the Y_2SiO_5 phase performed on the diffractogram of the HRTEM micrograph shown in (d) (the circled spots arise from the crystalline layer whereas other reflections are due to the adjacent YAG grains).

Table 4
EDX results from sample 1 (EDX spectra in Fig. 6c).

Atomic content of element (%)	Pure Y_2SiO_5 phase	Pure YAG $Y_3Al_5O_{12}$ phase	GB crystallite (EDX; Yb omitted)	Combination assuming a 33/66% balance of the Y_2SiO_5/YAG phases
O	62.5	60	61.0	61.0
Al	0	25	16.1	14.9
Y	25	15	17.4	19.0
Si	12.5	0	5.5	5.0

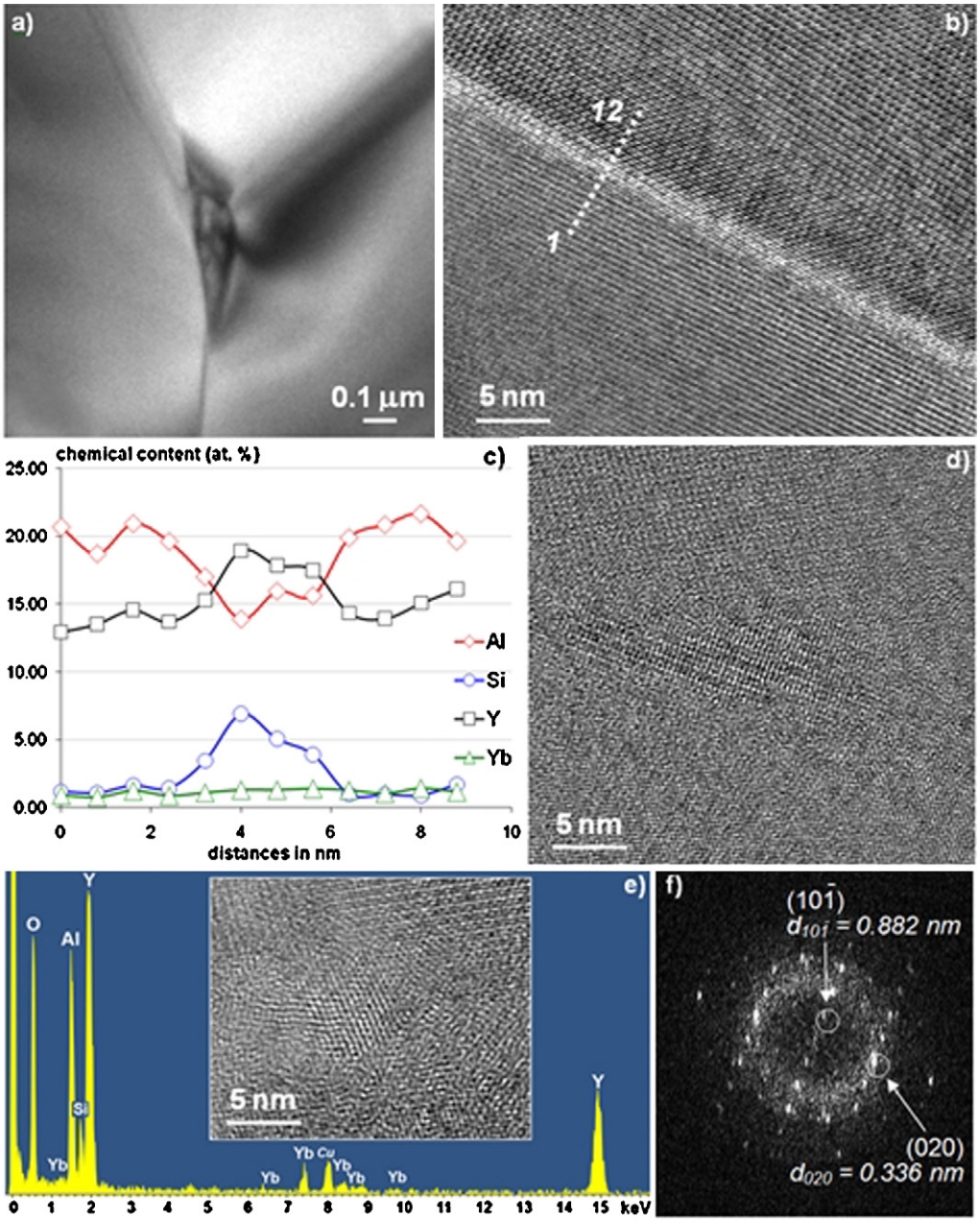

Fig. 7. Summary of TEM and EDX result for sample 2. (a) Representative triple grain junction showing a Y_2SiO_5 crystalline phase. (b) HRTEM lattice image of a phase-free grain-boundary; the dotted line shows the EDX line-scan performed across the boundary (12 measurements points with a probe of 2 nm in size). (c) EDX results of the line-scan analysis in (b). (d) Typical representative Y_2SiO_5 crystallite observed at a grain-boundary. (e) EDX chemical analysis of the intergranular precipitate shown in (d); insert is the aspect of the particle after analysis (see text for details). (f) Diffraction identification of the Y_2SiO_5 phase performed on the diffractogram from the HRTEM micrograph showed in (d).

smaller than the Y_2SiO_5 grains shown by the SEM preferentially in sample 1 as shown in Fig. 5(a).

It is interesting to notice that the structural evolution of the intergranular crystalline phase during TEM observation confirms the Si-enrichment of the grain-boundary. The inset in Fig. 7(d) shows the appearance of pure cubic Si (as attested by lattice fringes with a spacing of 0.31 nm corresponding to the Si {1 1 1} planes), due to electron irradiation induced damage of the Y_2SiO_5 phase.

The present TEM analyses also showed that ytterbium is homogeneously distributed within the microstructure, i.e. no Yb segregation at the grain boundary is observed.[16,17]

4. Discussion

The microstructure of the two samples described by the TEM analyses must be related to the role of the silica added to the system by means of TEOS as a sintering aid. TEOS was used in both samples to promote the sintering process through the formation of a liquid silica phase at the grain boundary that enhanced the mass transport by grain boundary diffusion, and therefore the densification with pore closure. The effect of silica on densification and microstructure evolution of doped YAG ceramic materials is reported by Stevenson et al.[9] Silicon oxide is obtained by the reaction of TEOS at $T > 600\,^{\circ}C$ that gives silica and diethylether:

$$Si(OC_2H_5)_4 \rightarrow SiO_2 + 2O(C_2H_5)_2$$

Silicon oxide forms a liquid phase at temperature >1400 °C. Boulesteix et al.[18] observed that the densification rate increases with increasing amount of silica as a result of both the decreased fractional solid–solid contact area and the enhancement of the kinetic of mass transport by diffusion through the liquid phase boundary during sintering. They showed as well[8] the presence of an intergranular inclusion of silica at triple points in YAG doped with 0.3 wt% SiO_2.

The samples presented in this study contain 0.5 wt% of TEOS that corresponds to 1.425 at.% of Si in YAG, lower than the solubility limit of Si in YAG at 1550 °C (1.5 at%) as reported by Sun et al.[19] The cooling rate of the sintering cycle is fast (about 50 °C/min from the sintering temperature down to 1000 °C) and consequently no major Si segregation at the grain boundaries would be expected. However silicon should segregate at the grain boundaries during the annealing cycle that is performed in air at 1300 °C for 0.5 h.

As far as it concerns the use of PEG during the mixing and shaping steps, it should not affect the behavior during sintering, since it burns out during the debonding cycle in air. However PEG improves the intimate mixing of the powders and the particle packing thus promoting the formation of a homogeneous microstructure with a regular distribution of the porosity and generally no large pore. The densification is hastened by these features, and under the same sintering conditions the samples with PEG often exhibit slightly larger grains and a more regular microstructure compared to those prepared with no dispersant. Even in the present case sample 1, prepared without PEG, exhibits a smaller average grain size. In addition in this sample the formation during sintering of large Y_2SiO_5 grains, that is thermodynamically favored,[20] occurred more extensively than in sample 2 because the powders were less intimately mixed (Fig. 5(a)). This condition lead also to a smaller amount of residual silicon within the YAG grains with respect to sample 2.

During the annealing cycle the silicon contained within the grains diffused towards the grain boundaries and at the triple points, where it eventually crystallized forming additional Y_2SiO_5 grains. The size of these Y_2SiO_5 grains however, is smaller than those formed during the sintering cycle, as shown by the TEM observation (Figs. 5(a) and 7(a)). In sample 2, thanks to the better particle packing, sintering lead to a more homogeneous microstructure and to larger YAG grains. On the other hand the larger grain size may slow down the Si diffusion out of the YAG phase during the annealing cycle. Moreover, the presence of a frequent thick silica rich intergranular phase in sample 1, not seen in sample 2 (compare Fig. 6(a) and Fig. 7(b)) indicate a larger silicon content at the grain boundaries in sample 1, thus a stronger depletion of this element within the YAG grains. All these arguments lead us to reasonably conclude that in sample 2 after the annealing a larger amount of silicon was still homogeneously dispersed within the YAG grains. This conclusion is hard to ascertain by direct EDX analysis of the Si content in the YAG host phase because: (i) this amount remains quite small (of the order of 1 at%), (ii) convolution of several excitation lines occur at the energy position of the Si–L transition (1.74 keV), where the Y–Ll and Yb–My lines are almost superimposed onto the Si signal (at 1.69 and 1.77 keV respectively, see for example Fig. 6(c)).

In recent literature the activation of non-linear change in the conductivity has been demonstrated in Yb doped active media in presence of high excitation level.[21] In particular the presence of Si or Fe impurities has been indicated as possible catalysts[22] for a cooperative energy transfer from three excited Yb^{3+} ions to an electron that is promoted in the conduction band, with an increase of conductivity and a corresponding loss of three excited ions and hence of radiative efficiency. The process is helped by Yb^{3+} high doping level and in general by high excitation density of the active ion.

The TEM analysis has excluded the presence of Yb segregation either near intergranular surfaces or at the triple points, and the content of Yb^{3+} ion is high enough to allow the activation of the cooperative energy transfer process. The presence of a higher concentration of Si within the grains in sample 2 highlighted by the present analysis, can explain the dramatic detriment of the radiative efficiency of this sample and thus what observed in the laser characterization. On the other side, the same analyses have evidenced in sample 1 the presence at the grain boundaries of a continuous amorphous Si-rich layer as well as of Y_2SiO_5 phase that easily explain the higher scattering coefficient of this sample in terms of refractive index discontinuity. The activation of non linear loss mechanisms have also been observed in samples with a quality near to the state of the art in presence of sufficiently high excitation density.[13]

In the same work an enhancement of the efficiency of the non radiative recombination channel has also been highlighted by increasing the doping level, consistently with a higher

probability of simultaneous participation of Yb ions to the loss mechanism. A combined role of thermal load at different density of the absorbed pump power cannot be excluded and will be investigated further.

5. Conclusions

A complete characterization has been performed on two transparent Yb doped YAG ceramics. Passive optical and laser characterizations have evidenced the positive effect of PEG as dispersant in order to achieve good optical quality of samples, while a nonlinear loss mechanism, triggered by the high spatial density of the excited ions, has been induced in the laser action. Thanks to the SEM and TEM analyses it has been highlighted that PEG can induce a higher concentration of residual silicon in the volume of grains associated to a bigger size of the grain themselves. The higher silicon concentration can act as catalyst for cooperative energy transfer with promotion of electrons in the conduction band and thus with consequent loss of excitation in laser operation. The thermal effects, which also are assumed to play some role in the activation of the loss mechanism, have to be investigated further.

Acknowledgment

Thanks are due to the CLYM (Centre Lyonnais de Microscopie – http://clym.insa-lyon.fr) for the access to the 2010F microscope.

References

1. Yanagitani T, Yagi H, Hiro Y. Production of yttrium aluminium garnet powders for transparent yag ceramic. Japan Patent, 10-101 411; April 21, 1998.
2. Ikesue A, Kinoshita T, Kamata K, Yoshida K. Fabrication and optical-properties of high-performance polycrystalline Nd–YAG ceramics for solid-state lasers. *J Am Ceram Soc* 1995;**78**(4):1033–40.
3. Nakamura S, Yoshioka H, Matsubara Y, Ogawa T, Wada S. Efficient tunable Yb:YAG ceramic laser. *Opt Commun* 2008;**281**(17):4411.
4. Zhou B, Wei Z, Zou Y, Zhang Y, Zhong X, Bourdet GL, et al. High-efficiency diode-pumped femtosecond Yb:YAG ceramic laser. *Opt Lett* 2010;**35**(3):288–90.
5. Pirri A, Alderighi D, Toci G, Vannini M. High-efficiency, high-power and low threshold Yb^{3+}:YAG ceramic laser. *Opt Express* 2009;**17**(25):23344–9.
6. Liu W, Jiang B, Zhang W, Li J, Zhou J, Zhang D, et al. Influence of heating rate on optical properties of Nd:YAG laser ceramic. *Ceram Int* 2010;**36**:2197–201.
7. Alderighi D, Pirri A, Toci G, Vannini M, Esposito L, Costa AL, et al. Characterization of Yb:YAG ceramics as laser media. *Opt Mater* 2010;**33**(2):205–10.
8. Boulesteix R, Maître A, Baumard J-F, Rabinovitch Y, Sallé C, Weber S, et al. The effect of silica doping on neodymium diffusion in yttrium aluminum garnet ceramics: implications for sintering mechanisms. *J Eur Ceram Soc* 2009;**29**(12):2517.
9. Stevenson AJ, Li X, Martinez MA, Anderson JM, Suchy DL, Kupp ER, et al. Effect of SiO_2 on densification and microstructure development in Nd:YAG transparent ceramics. *J Am Ceram Soc* 2011;**94**(5):1380–7.
10. Tsetsekou A, Agrafiotis C, Leon I, Milias A. Optimization of the rheological properties of alumina slurries for ceramic processing applications. Part II: spray-drying. *J Eur Ceram Soc* 2001;**21**(4):493–506.
11. Li W, Zhou S, Liu N, Lin H, Teng H, Li Y, et al. Effect of additives on optical characteristic of thulium doped yttria transparent ceramics. *Opt Mater* 2010;**32**(9):971–4.
12. Esposito L, Piancastelli A, Costa AL, Serantoni M, Toci G, Vannini M. Experimental features affecting the transparency of YAG ceramics. *Opt Mater* 2011;**33**(5):713–21.
13. Pirri A, Toci G, Alderighi D, Vannini M. Effects of the excitation density on the laser output of two differently doped Yb:YAG ceramics. *Opt Express* 2010;**18**(6):17262–72.
14. Caird JA, Payne SA, Staver PR, Ramponi AJ, Chase LL, Krupke WF. Quantum electronic properties of the $Na_3Ga_2Li_3F_{12}:Cr^{3+}$ laser. *IEEE J Quantum Electron* 1988;**24**:1077–99.
15. Joint Committee on Powder Diffraction Standards: Yttrium Silicate. *Powder diffraction (inorganic phases)*. Washington, DC: National Standard Bureau. Card No. 36-1476; 1989.
16. Chani VI, Boulon G, Zhao W, Yanagida T, Yoshikawa A. Correlation between segregation of rare earth dopants in melt crystal growth and ceramic processing for optical applications. *Jpn J Appl Phys* 2010;**49**: 075601–7.
17. Epicier T, Boulon G, Zhao W, Guzik M, Jiang J, Esposito L, Ikesue A. Spatial distribution analysis of the Yb3+ rare earth ions in optical oxide ceramics using TEM technique 2012, in preparation.
18. Boulesteix R, Maître A, Baumard J-F, Sallé C, Rabinovitch Y. Mechanism of the liquid-phase sintering for Nd:YAG ceramics. *Opt Mater* 2009;**31**(5):711–5.
19. Sun WY, Li XT, Ma LT, Yen TS. Solubility of Si in YAG. *J Solid State Chem* 1984;**51**(3):315–20.
20. Kolitsch U, Seifert HJ, Ludwig T, Aldinger F. Phase equilibria and crystal chemistry in the Y_2O_3–Al_2O_3–SiO_2 system. *J Mater Res* 1999;**14**(2):447–55.
21. Thornton SF, Bisson J, Kouznetsov D, Ueda K, Petermann K, Huber G. In: Conference on lasers and electro-optics/quantum electronics and laser science conference and photonic applications systems technologies, OSA Technical Digest Series (CD) (Optical Society of America, 2007), paper CFJ6; 2007.
22. Brandt C, Thornton SF, Petermann K, Huber G. Photoconductivity in Yb-doped oxides at high excitation densities. *Appl Phys B* 2011;**102**(4): 765–8.
23. Ahn CC, Krivanek OL. EELS Atlas. Tempe, AZ and Pleasanton, CA: ASU HREM Center and Gatan Inc.; 1983.